Chapter 6
Combinatorial Identification and Optimization of New Oxide Semiconductors

Bruce A. Parkinson

6.1 Background

The world must eventually shift from an energy economy primarily based upon fossil fuels to one based on renewable energy sources due to the eventual depletion of fossil energy supplies and concerns about climate change due to the accumulation of carbon dioxide in the atmosphere. Sunlight is the only renewable energy source that has the potential to provide the enormous amounts of energy required by the increasing population and economic development of the world. The production and efficiency of photovoltaic solar cells that produce high value electrical energy directly from sunlight are steadily increasing. However, electrical energy is not easily or economically stored. Since 75% of the world's present energy use is in the form of fuels, methods must be developed to transform solar energy directly into storable fuels. The photoelectrolysis of water directly with sunlight is the most promising method for achieving this result. Hydrogen, the most energy-dense fuel known, can be obtained from a readily available source and, when burned or used in a fuel cell, produces only water in a reversible cycle. Therefore, the development of a cost-effective method for splitting water directly with sunlight would pave the way to a future hydrogen economy, where no pollution or greenhouse gases are produced and that is based on a universally accessible energy source.

Current technology is capable of efficiently producing hydrogen from sunlight and water by connecting conventional solar cells to an electrolyzer [1]. The major disadvantage of this approach is that both of these devices are expensive. In addition, if the electrolyzer is not located near the solar cells, losses will be incurred during transmission of the electrical power, conversion from direct current to alternating current for transmission, and the voltage step-up and step-down at the solar array and electrolyzer,

B.A. Parkinson (✉)
Department of Chemistry and School of Energy Resources
University of Wyoming, Laramie, WY 82071, USA
e-mail: bparkin1@uwyo.edu

R. van de Krol and M. Grätzel (eds.), *Photoelectrochemical Hydrogen Production*,
Electronic Materials: Science & Technology 102, DOI 10.1007/978-1-4614-1380-6_6,

respectively. A potentially more efficient approach is to combine these two expensive components into an inexpensive single device that both absorbs the solar energy and performs the oxidation and reduction of water. In this approach, the generated hydrogen can be transported through pipelines (with significantly less loss than the present transport of electrical power on transmission lines) or in high-pressure tanks.

Although oxygen evolution was observed as early as 1968 when illuminating a rutile electrode in solution [2], application of this concept to water photoelectrolysis was first pointed out by Fujishima and Honda in a series of experiments that used the n-type semiconductor rutile form of TiO_2 [3, 4]. Although TiO_2 is stable under illumination in aqueous electrolytes, its large bandgap (3.0 eV) limits its utilization to the UV portion of the solar spectrum and thus limits its ultimate efficiency. It should also be pointed out that the conduction band of rutile is not negative enough to reduce water and so in the original publications a "pH bias" was present where the oxygen-producing side of the cell was basic with respect to the hydrogen-producing electrolyte. Later work using heterojunctions of III–V materials as photoelectrodes considerably increased the visible light conversion efficiency but also increased the cost and decreased the effective lifetime of the device due to corrosion in aqueous electrolytes [5]. Stability of a photoelectrolysis electrode is crucial for a viable system since the significant capital investment needed for the support structures, electrolyte handling and gas handling systems requires that the system last for many years. Since the photoelectrode will be continually immersed in an electrolyte and illuminated with direct solar radiation, a long lifetime is a daunting challenge that must be adequately addressed even in the basic research stages. It is primarily for their stability that metal oxide semiconductors arguably hold the most promise for constructing a stable photoelectrolysis system.

In addition to low cost and stability, any efficient photoelectrolysis material must also effectively utilize the solar spectrum and generate sufficient photovoltage to drive the water-splitting reaction. Either a single or tandem semiconductor electrode system may be used [6]. The obtained photovoltage must be greater than the thermodynamic value for the difference between the water oxidation and water reduction potentials (1.23 eV). The material(s) should have some catalytic activity for hydrogen or oxygen production so as to minimize the additional photopotential above 1.23 V that is required to overcome the electrochemical overpotentials needed to drive the water oxidation and reduction reactions at the desired rate. Current densities (rates) on the order of 15–25 mA/cm^2 at illumination intensities around 1 sun are also needed for a single photoelectrode system and half these values for a tandem system. In addition, a single semiconductor photoelectrode must have a valence band edge that is more positive than the water oxidation potential and a conduction band edge that is more negative than the water reduction potential so that the photogenerated holes and electrons have the electrochemical driving force for the water-splitting reaction. If a dual photoelectrode system is used, the conduction band of the p-type material must be negative of the water reduction potential and the valence band of the n-type material must be positive of the water oxidation potential.

As stated above, either a single semiconductor electrode or a two-semiconductor electrode photoelectrolysis system can be envisioned. The single illuminated

electrode system will need a bandgap greater than about 1.7 eV in order to supply the photovoltage needed for water photoelectrolysis given that photovoltage of about 2/3 the band gap is often the maximum obtainable from a good semiconductor material operating at its maximum power point. A single photoelectrode system would need to be attached to a catalytic metal (perhaps Pt or Pt modified) electrode that can accomplish the complementary water-splitting half reaction. A two-semiconductor system, with both a p-type and an n-type semiconductor photoelectrode, can be configured in several ways. In one configuration the electrodes could be placed with the larger gap material absorbing the higher energy portion of the solar spectrum in front of the smaller bandgap material of the opposite carrier type in which the wavelengths transmitted through the large bandgap material would be absorbed in the smaller gap material. The two materials must absorb nearly equal numbers of solar photons since the current through each semiconductor must be matched due to the recombination at the ohmic contacts that provides the summation of the two photovoltages. Therefore, in this configuration the quantum yield for water photoelectrolysis will be half that of a single photoelectrode system; however, since there is considerable photon flux in the red and near IR portion of the solar spectrum, the lower quantum yield may be offset by utilizing this portion of the solar spectrum. This configuration has the advantage that one glass substrate, with a transparent conducting layer on both sides, could be used for both materials reducing the total system costs. The ideal bandgaps for the two materials have not yet been identified but they will most likely be somewhat different than for a two-bandgap heterojunction solar cell where bandgaps of 1.9 and 1.2 eV give the best theoretical light to electricity conversion efficiency but yield a photovoltage larger than necessary for water photoelectrolysis. A larger photovoltage would provide some extra driving force for a photoelectrode that does have optimal catalytic properties for water oxidation or reduction. A schematic of a cross section of such a device is shown in Fig. 6.1. Systems that convert the extra photovoltage to electrical power can also be designed but the electrical power produced would most likely be more expensive than if produced from a conventional photovoltaic device.

Another configuration would be to place the n and p type materials side by side rather than putting a larger bandgap material in front resulting in full spectrum sunlight illumination for both electrodes. In this case, an n-type and p-type electrode of the same material or two different oppositely doped smaller bandgap materials can be paired as long as the sum of their photovoltages at maximum power was greater than the ~1.7 eV needed for water photoelectrolysis and the photocurrents in both electrodes were matched. If two materials were used the bandgaps would have to be close to each other since they need to absorb nearly the same flux of solar photons in order for the photocurrents to be matched. Two stable materials would be needed for this configuration to work, a p-type material with a conduction band at least 0.8 eV negative of both the n-type material conduction band and the hydrogen potential and valence band offsets of about 0.8 V. Two substrates would also be required, but they need not be transparent (as in the case of the stacked system discussed above and shown in Fig. 6.1) and so

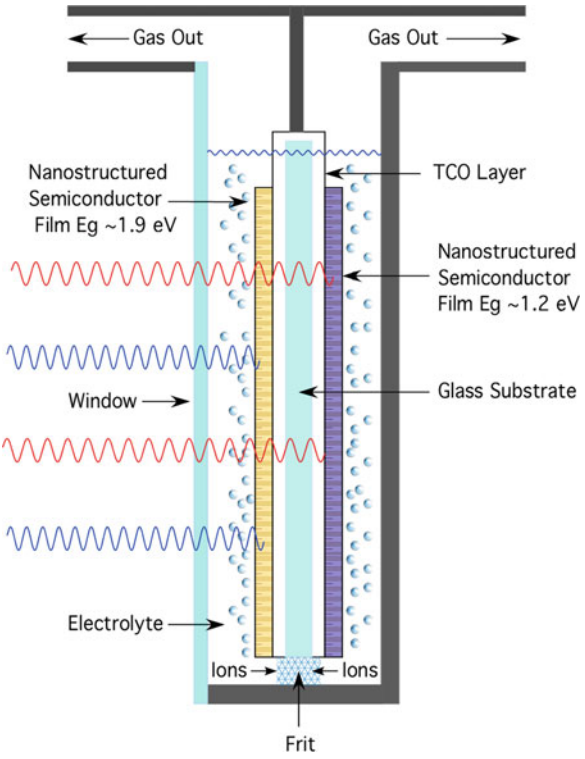

Fig. 6.1 A design for a tandem photoelectrolysis system that uses nanostructured semiconductor films of opposite carrier type that are deposited on opposite sides of a single substrate that is covered on both sides with a continuous transparent conducting oxide film. The larger bandgap material is transparent to the lower energy radiation that is absorbed by the smaller gap film on the backside of the substrate

cheaper and more abundant materials may be utilized. Table 6.1 summarizes the advantages and disadvantages of the different photoelectrolysis configurations discussed above. Systems that contain buried junctions, where charge separation is remote from the electrolyte, are really solid state solar cells in series with metal electrodes, are not considered since they are essentially equivalent to hooking up photovoltaic cells to an electrolysis cell.

Any photoelectrolysis system will have to be designed with an ion conducting separator or electrolyte path between the two electrodes and with separate gas collection plumbing for hydrogen and perhaps oxygen. Oxidation reactions, other than water oxidation, have been discussed since there is much less demand for pure oxygen than there is for hydrogen. The commercial demand for pure oxygen would be rapidly saturated once any water-splitting photoelectrolysis system with the capacity to produce meaningful amounts of hydrogen is deployed. The only other commercial chemical currently produced on a very large scale by aqueous electrolysis is chlorine, but again the demand for chlorine would be quickly met by any system producing enough hydrogen fuel to make an impact on world energy demand. However, photoelectrolysis technology could get an initial boost from the additional revenue obtained from the photoelectrolysis of hydrochloric acid or brine.

Table 6.1 A comparison of the advantages and disadvantages of various configurations for a photoelectrolysis device

Configuration	Advantages	Disadvantages
Single photoelectrode	Only one substrate and one p or n type semiconductor needed. Dark electrode can be conventional.	Poor utilization of the solar spectrum since large bandgap (>~1.7 eV) is needed.
Tandem photoelectrodes (Fig. 6.1)	Needs only one substrate. More efficient utilization of the solar spectrum.	Need to identify one p and one n type semiconductor and needs a transparent conducting substrate. Two photons and current balancing needed.
Separately illuminated photoelectrodes	Cheap nontransparent substrates can be used. More efficient utilization of the solar spectrum.	Need two semiconductors or ability to dope one both n and p type. Two photons and current balancing needed. Twice the collector area of tandem.

Often materials are synthesized and tested for photochemical water-splitting activity as either colloidal solutions or as powdered slurries. While this method may be useful for screening for water-splitting activity, it is unlikely that homogeneous colloidal solutions or slurries will be useful for a practical water-splitting system. Several reasons for this include (1) The products are not produced in separate compartments, resulting in highly explosive mixtures of hydrogen and oxygen. (2) Energy is required to separate hydrogen and oxygen reducing the overall efficiency of the water-splitting process. (3) Since catalysts for hydrogen and oxygen production from water are also good catalysts for the recombination of hydrogen and oxygen, illumination of such systems will eventually result in a photostationary state where forward and back reactions have equal rates and no more water splitting can occur. The exchange current at the photostationary state will be related to the solubility of the gases in the electrolyte and the rate at which they are removed from the reactor.

To avoid undesirable back reactions, and the poor kinetics for hydrogen or oxygen production, sacrificial reagents are often used in the photoreactors to scavenge either holes or electrons. The most common examples of hole scavenging agents introduced into solution are alcohols (usually methanol), amines (usually triethanolamine or EDTA), or sulfite salts. Electron scavengers such as the easily reduced Ag^+ can also be added. Electron or hole scavengers can be useful to study *one* of the water-splitting half-reactions without complications associated with the kinetics of the other half-reaction (although using a three-electrode potentiostat to study a single photoelectrode would achieve the same end) but these additives are not viable for any practical system for sustainable energy production.

As a comprehensive review of photoelectrochemical hydrogen generation [7] and a recent book [8] have been published on this subject, this chapter will concentrate on the combinatorial aspects of the search for appropriate materials for a practical device.

6.2 Survey of Known Materials and Their Photoactivity

As discussed above, the positions of the conduction band and valence bands with respect to water oxidation and reduction potentials are one requirement for a water-splitting photoelectrode. Among the first materials to be exhaustively studied were the perovskite structure oxides $SrTiO_3$ [9–13] and $BaTiO_3$ [9, 14, 15]. Both of these materials are better suited than TiO_2 for water photoelectrolysis because their conduction band edges are more negative than the water reduction potential. Unfortunately, as is also true for TiO_2, their bandgaps are so large (~3.2 eV) that they also required UV light to produce photocurrent resulting in very poor solar efficiencies.

A practical solar photoelectrolysis material must also be stable under illumination for many years while immersed in an aqueous electrolyte. Photocorrosion is the main problem with nonoxide semiconductors that have near optimum band gaps [16] and band positions for efficient photocatalytic water splitting such as transition metal chalcogenides [17–19], cadmium and zinc chalcogenides, GaAs [20], GaP [21], and InP [5, 22–24]. Thermodynamic stability is assured only if the oxidation decomposition potential of the semiconductor is more positive than the valence band edge and the reduction decomposition potential lies more negative than the conduction band edge [25]. Because the redox potentials for the decomposition reactions of these materials are generally within the band gap, and additionally because the decomposition reactions are kinetically favored, these experiments generally lead to electrode photocorrosion. If even only a tiny fraction of the photoexcited carriers are involved in photocorrosion reactions the electrode will not survive for many years under solar illumination intensities.

The most stable rocks and minerals that survive many years of weathering are all oxides, suggesting that a semiconducting oxide material will have the best chance to fulfill the stability criteria for a water-splitting photocatalyst. Smaller bandgap metal oxide semiconductors, notably WO_3 [26–29], Fe_2O_3 [30–35], NiO [36, 37], and Cu_2O [38], have also been extensively studied. Although these materials harvest a larger percentage of the solar spectrum, their conduction band edge energies are often not optimally positioned for the production of hydrogen [39]. They can also be difficult to electrically dope, resulting in being either poor conductors of electrons and/or holes and some of them (e.g., Cu_2O) are still prone to corrosion [16].

The valence band positions of oxide materials are usually similar and quite positive due to the fact that the band is derived from oxygen 2p states. Holes at such a positive potential can easily oxidize water but can waste considerable energy in doing so either due to the large difference in potential between the holes and the water oxidation potential or poor electrochemical kinetics for water oxidation. One idea to both extend the spectral response of large gap oxide semiconductors and to raise the valence band energy is to incorporate sulfur, carbon, or nitrogen into the lattice. A series of these compounds including $Sm_2Ti_2S_2O_5$ [40], TaON [41], $Y_2Ta_2O_5N_2$ [42], Ta_3N_5 [43], and $LaTiO_2N$ [44, 45] as well as incorporating S, N, or C into TiO_2 [46–49] have recently been examined by several research groups. These groups often use density functional theory to calculate that the bottom of the

conduction bands consists of empty d-orbitals and, depending upon the material, the tops of the valence bands consist mainly of N 2p or S 3p orbitals resulting in smaller band gaps for improved solar energy utilization. The smaller band gaps, and fortuitous band positions relative to the redox potentials of water, imply that these materials could function as water photoelectrolysis materials; and indeed H_2 and/or O_2 is produced at quantum efficiencies up to 30% [41]. Unfortunately, however, most of these systems are typically not reported to function without the presence of the "sacrificial reagents" in solution mentioned earlier. It is likely that the sacrificial reagents are necessary to camouflage inherent oxidation or reduction decomposition reactions and that these materials will ultimately have the same stability problems as the earlier materials that incorporated nonoxide anions since nitrogen, sulfur and carbon are easily oxidized in solution.

In principle, if one introduces an additional metal or metals into the structure that have electronegativities greater than that of the parent metal and less than that of oxygen, then it is possible that a valence band created from mixed metal d states will be more negative in energy (closer to the oxidation potential of water) than that of a pure oxygen 2p band, thereby reducing the bandgap to 1.5–2.0 eV [50]. As an example, a mixed metal oxide semiconductor could be constructed with conduction band edge derived mainly from titanium. In principle, it should then be possible to create mixed bands, lowering the band gap of the parent titanium oxide, by mixing the transition metal orbitals with the oxygen 2p orbitals. For example, the ions Mn^{2+}, Ni^{2+}, Cr^{3+}, Rh^{3+}, V^{4+}, Os^{3+}, Sn^{2+}, Sb^{3+}, Pd^{2+}, and Pt^{2+} all have d orbital energies that are more positive (further down an absolute scale) than the oxidation potential of water but more cathodic than that of oxygen's 2p orbital [50]. And so, in theory at least, by combining these metals with titanium it should be possible to create a material with a band gap can absorb a large fraction of the solar spectrum and is optimally positioned to photoelectrolyze water. Other compositions such as $LuRhO_3$ [51], $SrZr_{0.25}Ti_{0.75}O_3$ [50], $LaVO_3$ [52], $K_2La_2Ti_3O_{10}$ [53], and $RbPb_2Nb_3O_{10}$ [54], have also been reported to be viable photoelectrolytic systems and provide useful starting points in a combinatorial search.

6.3 Combinatorial Production and Screening of Metal Oxide Photocatalysts

Multicomponent materials are often required to optimize a special property. High temperature superconductivity is a good example of a special property requiring multicomponent materials. The oxide with the highest known transition temperature contains four or even five metals ($HgBa_2CaCu_2O_{6+d}$, $Hg_{0.8}Tl_{0.2}Ba_2Ca_2Cu_3O_{8.33}$, $T_c \sim 125$ K). Since our present theoretical knowledge is insufficient to a priori calculate the behavior of such complex systems, or estimate the identity and atomic ratios of the specific metals needed to perform the efficient photoelectrolysis of water, empirical methods will be necessary to identify the best material. Thousands, or perhaps hundreds of thousands, of mixed metal oxide photocatalyst compositions

may need to be produced and tested for efficiency and corrosion resistance until an effective material is discovered. Fortunately, the recent development of combinatorial methods has provided tools for the production of large libraries of compounds and the methods for screening these libraries for the presence or optimization of a property of interest. In this section, we will review the combinatorial approaches that have been applied to the discovery and optimization of water-splitting photocatalysts.

We can first do an analysis of the number of possible combinations of mixed metal oxides that could be produced and screened. If we prepare all possible ternary oxides, mixing N materials three at a time there are $N!/3!(N-3)!$ combinations if we only consider 1:1:1 stoichiometries. Since there are ~60 possible candidate metals in the periodic table this results in >34,000 combinations to be produced and tested. If a quaternary material is needed then there are $N!/4!(N-4)! > 480{,}000$ possible combinations. Again these numbers do not consider producing and screening the many possible stoichiometries. It is also possible that a ternary or quaternary material will require small amounts of an additional element that acts as an electrical dopant to optimize its conductivity. These small amounts can often exist as impurities in the metal oxide precursors or may have to be discovered by additional combinatorial screening (discussed later in this chapter) greatly multiplying the number of experiments that must be done. However, some combinations could be excluded because it would not make sense to, for example, mix only large bandgap oxide materials (i.e., Ti–Zr–Si–Y oxides) and expect visible light absorption. It is clear that given the large number of possible mixtures that need to be produced, a "high-throughput" approach is needed, as well as multidimensional experimental design, to explore the parameter space more rapidly. And while it may not be reasonable to produce and test ALL of the possible combinations, it is certainly imperative that the throughput of materials screening be rapid relative to the serial approaches that have historically been used.

We can also use some chemical knowledge to reduce the number of combinations that need to be tested. We can very loosely classify metals into one of four categories according to their potential role in a photoelectrode material; structural, since they form very stable high heat of formation oxides (i.e., Ti, W, Zr, Ta, Si, Mo, Nb, Hf, In, Sn, Y, Sc whose oxides have very high bandgaps and so are not useful by themselves), light absorbing, where multiple elements may be needed to absorb light across the solar spectrum [55, 56] (i.e., Fe, Cr, V, Co, Mn, Ni, Cu, and some rare earths such as Ce), catalytic, to lower overpotential losses in the electrochemical reactions (i.e., Ru, Rh, Pd, Ni, Pt, Ir, Os, Re) [55, 57, 58] and ionic charge compensators (i.e., Ca, Sr, Ba, Mg, Zn, Cd, Li, Na, K, Rb, Cs)[1] that are often present in stable structures such as spinels and perovskites to balance the charge in the compound since oxygen is almost always present in stable oxides as O^{2-}.

[1] We purposely do not include toxic metals such as Pb, Tl, Cd, and Hg since we envision eventual large-scale implementation of any discovered photocatalysts and we want to avoid the environmental consequences of these elements.

This chemical guidance greatly reduces the number of possible combinations (but it is still in the tens of thousands). Finally, it may be necessary to deposit catalytic materials such as Pt, Pd, Ir, Ru, or Ni [59–61] or small molecule catalysts onto the surface of the electrode if the surface of the semiconductor itself has little catalytic activity.

With the appropriate substrate a combinatorial library can be tested for photoactivity by a number of different methods. While the ideal method would be to *directly* measure hydrogen production with, for example, gas chromatography, the amount of hydrogen expected to be produced from a thin film photoelectrode that does not absorb a large fraction of the incident light (the reason for very thin films is discussed below) is typically too small to generate hydrogen at a rate needed to overcome the solubility of the gas in aqueous solution. In light of this limitation, screening for photocatalytic activity has largely been carried out by measuring spatially resolved photocurrents or by observation of pH changes in the electrolyte near the array.

The use of pH-dependent fluorescent indicators [62] or molecular sensitizers [63] is based upon the principle that the local concentration of protons increases at sites catalytically active for water oxidation (oxygen production) and decreases at sites active for water reduction (hydrogen production). The reverse processes of hydrogen oxidation or oxygen reduction also cause a change in pH making the method useful for screening fuel cell catalysts as well as photoelectrolysis catalysts. A visual or CCD camera inspection of an irradiated catalyst library can be sufficient to ascertain activity if the amount of redox chemistry and/or the fluorescence of the indicator is sufficient. Otherwise, a spatial analysis of absorbance or emission changes must be carried out. The advantage of this approach is that it is a rapid detection method and avoids some of the spurious signals that can result from electrochemical detection methods. On the other hand, it is not high resolution and one must assume that the indicator molecules do not interfere with the overall redox process occurring in solution (such as competitive charge transfer to the indicator in lieu of photocatalysis) and the appropriate indicator must be found for the chosen electrolyte. Alternative screening techniques with higher resolution will be described in the following section.

6.4 Methods for Combinatorial Production and Screening

6.4.1 Inkjet Printing and Electrochemical Scanning Light Beam Analysis

Inkjet printing has been utilized for many combinatorial chemistry applications including the production of luminescent metal oxide libraries [64]. The hallmarks of inkjet printing for materials deposition are its speed, ease of use, low cost (depending upon the printing platform chosen) and its versatility. The combinatorial search strategy within our group [58], and later adopted by the Lewis group [65],

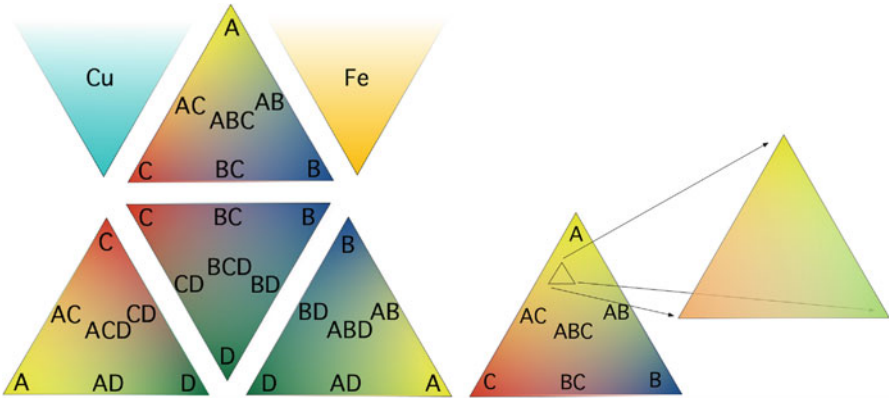

Fig. 6.2 The faces of a four-component tetrahedral phase diagram where the four metals are mixed three at a time in triangles that correspond to ternary phase diagrams. When a promising composition was found, for example, the small triangle inset of the ABC ternary mixture on the right, the gradients could be adjusted to expand that region of the ternary phase diagram and the necessary number of iterations could be performed until the best mixture is found. Copper oxide and iron oxide are also printed in a gradient triangle as p and n type simple oxide internal standards, respectively. Mallouk et al. used this scheme for screening of precious metal fuel cell catalysts [62]

utilizes inkjet printing of overlapping patterns of soluble metal oxide precursors onto a conductive substrate. Metal nitrate salts have been the most widely printed precursors since they are highly soluble and subsequent pyrolysis at temperatures below 550°C yields metal oxides. Temperatures must be kept below about 550°C since above these temperatures the glass begins to soften and the conducting FTO layer becomes unstable.

Our work has used a research grade printer manufactured by FujiFilm Dimatix [58] and off-the-shelf consumer grade printers made by Hewlett Packard [66]. Originally, films were deposited in overlapping triangular gradient patterns as shown in Fig. 6.2.

While inkjet printing such a pattern ideally produces smooth gradients in composition, in reality the extent of uneven mixing of compositions within the triangles can be unknown. Assuming that the actual deposition amounts of the material precursors is linear from the vertices to the edges of the triangle, other factors such as miscibility, phase segregation, annealing effects, etc., might also play a role and make it difficult to know the exact composition in a particular spot. One particular complication that has emerged during our studies is that the metal nitrate salts generally melt before they decompose and coalesce into droplets, resulting in less uniform films of the oxide after pyrolysis. The use of metal oxide nanoparticles, polyoxometalates, and various alkoxide compounds as precursors that decompose directly into the oxide will be useful to avoid this complication.

To analyze for photoelectrolysis activity several groups use custom-built scanning laser screening systems where a laser is rastered over the printed and pyrolyzed substrates that are immersed in an aqueous electrolyte. Scanning the

laser over the sample produces a false color image of photoactivity by measuring the photocurrent at each "pixel." To detect small signals the laser can be chopped or modulated and a lock-in amplifier can be used to isolate the photocurrent signal even if there is substantial dark current present. A potentiostat can also be used to apply a positive or negative external bias to the sample to aid the oxidation or reduction of water, respectively. The external bias will not be useful for a practical system but is used so that a good semiconducting material that might not be electrocatalytically active may still be identified and can have a surface catalytic layer added later.

Figure 6.3 shows a template, a photograph, a false color photocurrent image and a false color photocurrent image of a compositional zoom of a promising compositional region. In the false color photocurrent images in Fig. 6.3, the yellow to white pixels corresponds to higher relative photocurrent where a Fe–Cs–Nd composition is most photoactive. The dark blue regions represent areas where there is virtually no photoactivity either from the FTO substrate or the material. Also printed and screened using this template are n- and p-type "internal standards" of a-Fe_2O_3 and CuO, respectively, printed because it not only affords a direct comparison to these well-known semiconducting oxide materials [20], but also between all printed sample plates.

Hundreds of materials have been produced and screened using the unfolded tetrahedron template, with most of the material combinations showing no or very little photoresponse but some showing significantly better performance than the internal reference materials. One of the materials discovered in our search, composed of Fe, Co, and Al, has reproducibly shown p-type photoactivity and was not previously known to function as a photoelectrolysis material. The regions of high activity were found in the Co-rich regions of the Co–Al–Fe triangles. While this original high-throughput method was useful for identifying promising materials, the exact stoichiometry of the metal components in the active mixture was uncertain since the exact amounts of the various "inks" delivered by the printer driver software is unknown.

In order to determine the optimum stoichiometry of the promising mixture, a series of samples with an array of areas with known compositions was prepared using a research grade inkjet printer manufactured by FujiFilm Dimatix. This printer has a camera that focuses on the printhead nozzles and software control of parameters such as the waveform applied to the piezoelectric jetting nozzle, drop spacing, drop volume, and jetting frequency. By controlling these parameters, production of a broad or narrow compositional range with known stoichiometries within each printed area is possible. The thickness of each sample can also be controlled with these factors or, if desired, by depositing multiple layers. An example of a sample plate prepared in this way is shown in Fig. 6.4. In this pattern, four different densities of Co and Fe were printed as double horizontal and double vertical rows, respectively, while different amounts of Al were deposited in a repeating pattern within groups of four squares containing identical Fe and Co amounts as shown in the dashed inset in the upper left-hand corner. The precise values of the drop spacing and density printed within each square in

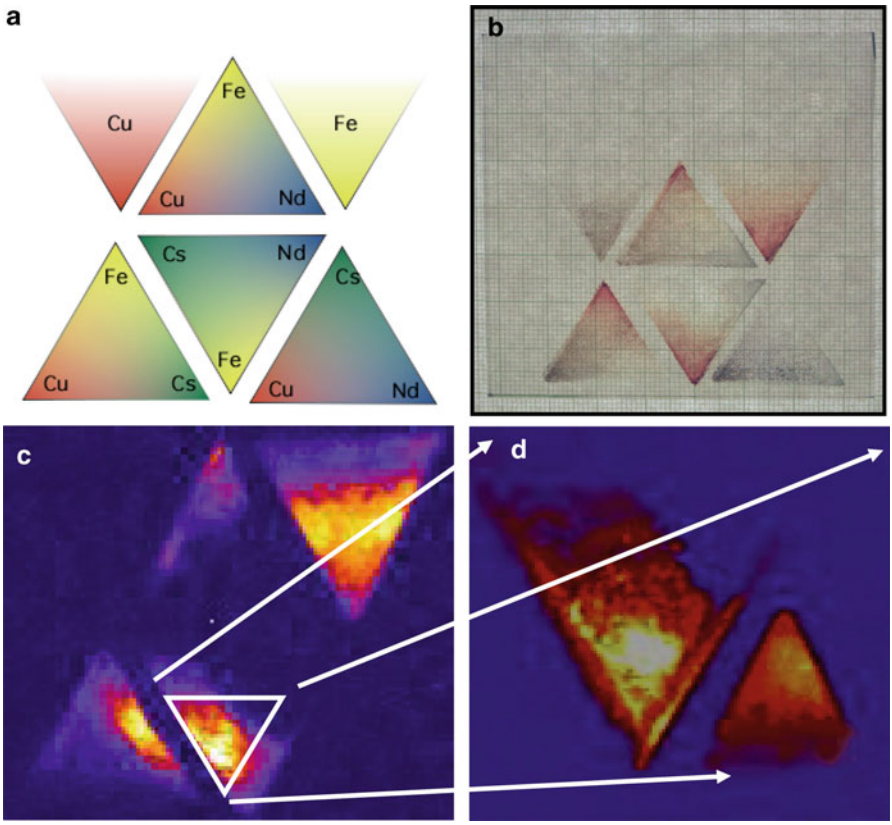

Fig. 6.3 Printing and screening a four-metals-three-at-a-time pattern and a compositional zoom for a Fe–Cs–Nd–Cu system. (**a**) False color template showing the positions and gradients used for printing the four metal precursor solutions. (**b**) Photograph of the printed and fired film. Note the triangular internal standards of a-Fe_2O_3 and CuO (*upper right* and *left*, respectively) with thickness gradients (*bottom* to *top*) that are used as internal standards. (**c**) False color photocurrent image of the film shown in B using 514.5 nm illumination under 0.5 V bias in a 0.5 M NaOH solution. The photocurrent produced at a particular "pixel," relative to the others in the two-dimensional array, is represented by its relative brightness with the most photocurrent in a particular direction (water oxidation in this case) being the brightest. (**d**) Photocurrent scan at 514.5-nm of a triangular composition zoom in on the brightest area of the Fe–Cs–Nd triangle shown in (**c**) that has a maximum IPCE value approximately twice that of the a-Fe_2O_3 internal standard (*smaller triangle* to the *lower right*). Expanding the printing gradients within the brightest region of the n-type material created the "zoom in." Reproduced with permission from [66], copyright 2005 American Chemical Society

Fig. 6.4 for the Fe and Cu internal standards, as well as the Fe–Co–Al Oxide precursors, can be found in reference [66]. As an example, the brightest square in Fig. 6.4, third square from the right, third row down, is given the label $Fe_BCo_DAl_A$ which correlates to $Fe_{1.7}Co_{14.4}Al_1$ (In atomic percentages 10% Fe, 84% Co, and 6% Al) and this composition was used in future photoelectrochemical and structural

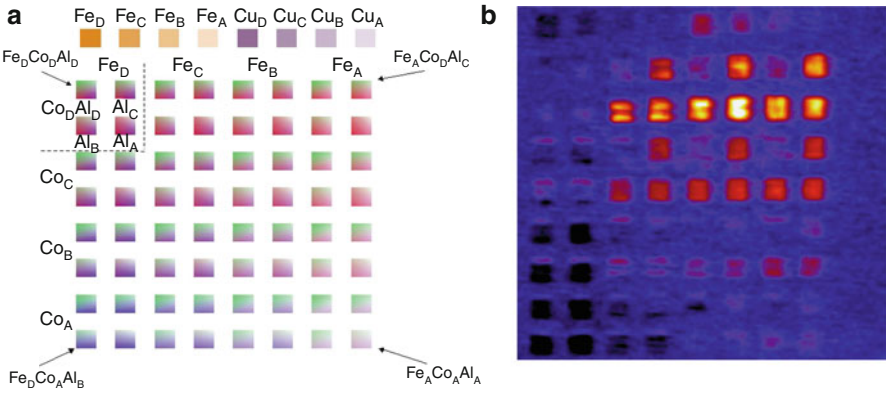

Fig. 6.4 (**a**) Printing template used for quantifying the optimal stoichiometry in the Co–Al–Fe system where known amounts of the components are printed into individual 3 × 3 mm^2. The density of precursor drops (and the resulting stoichiometry) corresponding to each stoichiometry for different thickness is described in reference [58]. (**b**) False color photocurrent map with no applied bias with 532 nm laser excitation in a 0.1-M NaOH solution. The cathodic photocurrent measured by laser scanning the brightest square of the film is nearly three times that generated by the best pure CuO internal standard labeled Cu_D. The compositions within the solid white box were expanded in Fig. 6.5. Reproduced with permission from [58], copyright 2008 American Chemical Society

experiments where bulk samples were prepared as it consistently appeared to be a near optimal composition.

In contrast to the "zoom in" shown in Fig. 6.3, created by adjusting the printed gradients, the most promising stoichiometries within array-based samples can be investigated much more quantitatively. To further refine the optimal composition of the photocatalyst described above, another template was created that encompasses stoichiometries outlined by the white triangle as well as some similar stoichiometries. The template, and the result of the photocurrent screening, is shown in Fig. 6.5. In this pattern, the amount of cobalt was kept constant (labeled B in the figure with a drop spacing equal to that of all mixtures within the white box of Fig. 6.4) while the Fe and Al contents (labeled w, x, y, and z) were varied and calculated using the rationale described previously. The internal standards were printed with the same drop densities as in Fig. 6.4 and the overall amount of printed internal standard material relative to the working mixtures is approximately the same between Figs. 6.4 and 6.5 in order to not overestimate the contribution of sample thickness to performance. The resulting photocurrent for all working Co–Al–Fe oxides is within ±20% for all squares indicating flexibility in the stoichiometries of the photoactive compositions. Indeed, the Fe and Alcontent can vary by as much as a factor of two (between $Co_{17.8}Fe_1Al_{2.1}$ and $Co_{17.8}Fe_{2.1}Al_1$) and still produce a material with comparable photoactivity.

Currently inkjet printing allows one to rapidly produce and screen many materials and quantify the most promising stoichiometries. Lewis, Katz and Gingrich [65] have devised a variation of the technique described above that allows

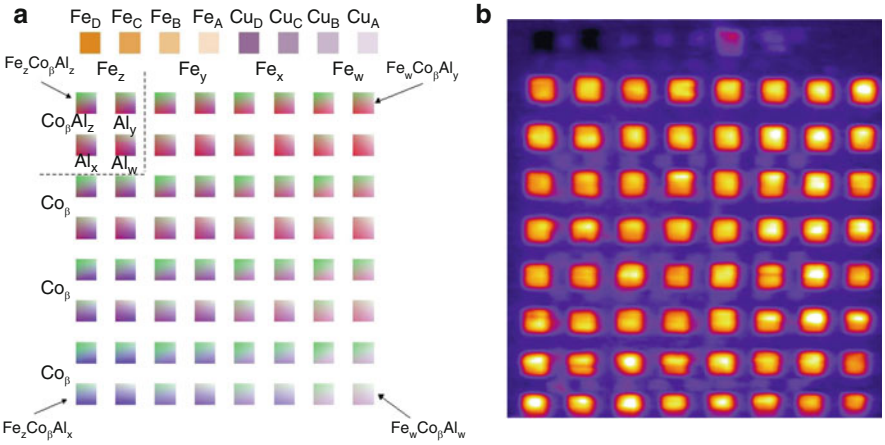

Fig. 6.5 Compositional library produced by expansion of the compositional region outlined by the white box in Fig. 6.4. The template shown in (**a**) was created by including all of the mixtures created within the inset of Fig. 6.4 as well as some intermediate stoichiometries. The pure Fe and Cu internal standards were printed as in Fig. 6.4. (**b**) Photocurrent map of the array of 3×3 mm^2 measured in 0.1-M NaOH with a 532-nm laser showing that a rather large range of composition space appears to work better than the CuO internal standards. Reproduced with permission from [58], copyright 2008 American Chemical Society

for the measurement of the open-circuit photovoltage as well as the photocurrent response of each composition. The photovoltage provides a valuable estimate of the position of the quasi-Fermi level of the majority carriers under illumination, which indicates whether the photogenerated carriers are thermodynamically capable of a particular photoelectrolysis reaction. Since the photovoltage measurement is for the entire electrically connected substrate, to measure it for a specific area or composition requires electronic isolation of each metal oxide mixture, as well as passivation of the exposed conductive substrate. To achieve this up to 260 regions on the FTO substrate are laser etched to remove the FTO from the regions between the areas to be printed and electrically isolate them. Up to eight precursors are then printed in the isolated regions and pyrolyzed. An insulating epoxy is then screen printed over any exposed FTO. A multiple contact connector is then clamped to the substrate and connected to a custom-designed printed circuit board where each contact on the circuit board is associated with a particular spot in the materials library and connected through ribbon cables to a multiplexer for the electrical measurements.

The Sayama group also currently utilizes a scanning light beam analysis system for high-throughput screening of photoelectrolysis materials [67]. In their system the libraries are produced by an automated robotic pipetting of precursors onto a substrate with a subsequent firing. The photocurrent of each sample in an array is then measured at a constant potential in a three-electrode cell by scanning the photoelectrode with a focused beam from a xenon lamp guided by an optical fiber with a UV cutoff filter. Their high-throughput production and screening system has been used to optimize the stoichiometry of some porous iron oxide binary compositions.

6.4.2 Combinatorial Dopant Optimization Using Inkjet Printing

Low levels of impurities are well-known to control the electrical properties of semiconductors via electrical doping or to produce potent deep trap states that can promote carrier recombination and destroy the photoresponse of the material. It is often difficult to control or determine these low levels of active impurities; however, in some photoelectrode materials purposely adding impurities can dramatically improve the photoresponse. One such material, hematite (α-Fe_2O_3), has received much attention because of its bandgap of 2.2 eV, abundance, nontoxicity, and electrochemical stability. Many methods have been investigated to improve the photoelectrochemical performance of α-Fe_2O_3 including the incorporation of various other elements into the hematite films. Grätzel found that the introduction of a small amount of Si into the film dramatically increased the photooxidation current. Many other "dopant" species have also been added including Ca^{2+}, Mg^{2+}, Cu^{2+}, Zn^{2+}, Si^{4+}, Ge^{4+}, Ti^{4+}, Pt^{4+}, Cr^{4+}, V^{5+}, Nb^{5+}, and Mo^{6+} [68–82]. A number of these elements have improved the photoresponse of α-Fe_2O_3 but the mechanism for the enhancement has not often been explained. Some reasons for improvements of the photoactivity from adding impurities include lowering the resistivity of the film due to an increase in the majority carrier density, improvements in the electrocatalytic activity for water (OH^-) oxidation, directing the morphology of the film (nanostructuring) to allow more carriers to reach the semiconductor/electrolyte interface, passivating grain boundaries or producing different crystallographic orientations of the α-Fe_2O_3 crystallites to favor the growth of faces with a lower surface recombination velocity. The use of the term "dopants," when referring to the addition of more than parts per thousand levels of impurities, does not conform to the usual semiconductor physics definition of electrically active shallow dopants that can control the electrical conductivity at the level of parts per million. However, since this term has come into wide use, even when adding amounts of elements at levels more properly called solid solutions (if in fact all the additive is incorporated into the lattice), we will continue to use the term "doping" with the understanding that the reason these added elements influence the photocurrent and/or photovoltage are not usually known.

Given the multitude of possible enhancement effects, adding multiple elemental impurities might result in synergistic effects and produce films with much higher photoactivity than with just one impurity. However, given now the large number of possible additives at multiple concentration levels the number of samples that must be prepared becomes very large. Therefore, we adapted our inkjetting technique to quickly produce many "doped" α-Fe_2O_3 compositions and screen them for their water photooxidation activity. Since we will be printing arrays of α-Fe_2O_3 we first optimized the thickness of printed films of this material by varying the drop density and the number of times we overprint the pattern. An 8×8 array of squares was printed onto SnO_2:F-coated glass with 0.5 M $FeCl_3$ with drop spacing of 80 μm. This pattern, shown in Fig. 6.6a, was divided into four double rows printed once, twice, three times, and four times from the bottom to the top, to determine the

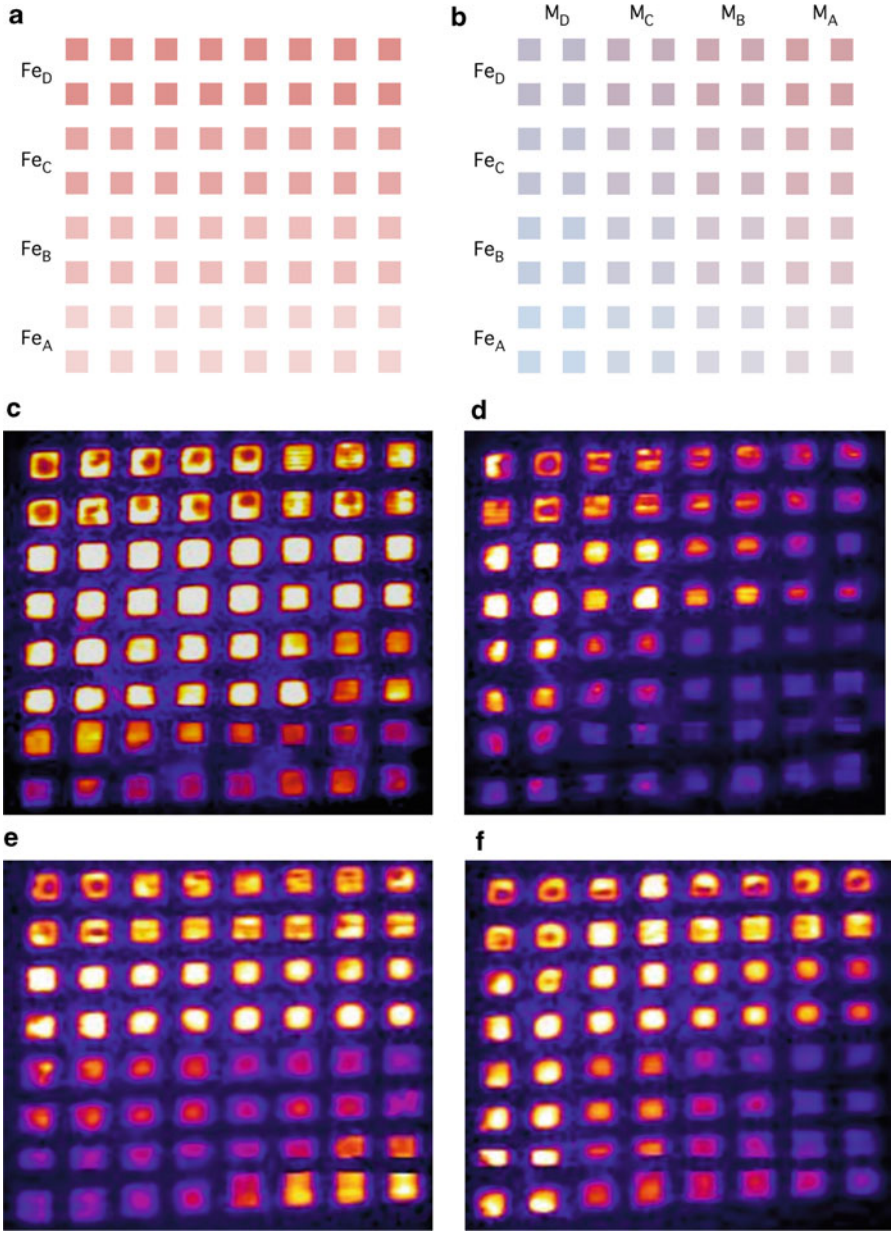

Fig. 6.6 (**a**) Printing template used for undoped α-Fe_2O_3 with ~80 μm drop spacing and double rows printed from the bottom up: once, twice, three times, and four times corresponding to Fe_A to Fe_D. (**b**) Printing template used for the Fe–M (M = Ti, Si, or Al) series where known amounts of the components are printed on top of the Fe rows from (**a**) into individual 3 × 3 mm^2 resulting in groups of four squares with identical compositions. The density of precursor drops and resulting stoichiometries for (**d**–**f**) are listed in Table 6.2. False color photocurrent maps of libraries printed using template (**b**): (**d**) Ti-doping; (**e**) Si-doping; (**f**) Al-doping. All libraries were scanned at 532 nm with +0.6 bias in a 0.1-M NaOH solution. Note that the false colors are relative within a scan and not absolute values therefore comparisons of color between scans are not quantitative. Refer to Table 6.3 for more quantitative comparisons

Table 6.2 Density of printed precursor drops used to produce libraries shown in Fig. 6.6d–f

			Relative stoichiometry (FeM_x)			
Row label	1D DS (μm)	Drops per mm^2	Column D	Column C	Column B	Column A
D	40	642	0.0067	0.0017	0.00078	0.00047
C	79	169	0.025	0.0067	0.003	0.0018
B	120	75	0.057	0.015	0.0067	0.004
A	160	45	0.095	0.025	0.011	0.0067

DS drop spacing

optimum α-Fe_2O_3 thickness for the maximum photocurrent signal. It was found that printing this concentration of $FeCl_3$ three times gave the best photocurrent signal (Fig. 6.6c). The top double row (Fe_D) was too thick resulting in darker areas in the center of the squares and bright edges due to the film being slightly thinner near the edges. The short diffusion length of carriers in this material results in decreases in photocurrent when the film is too thick. Note that in all cases most of the light still passes through the very thin film of α-Fe_2O_3 and so incident photon current efficiency (IPCE) values are low.

According to the literature [68, 72, 83], the addition of small amounts of Ti, Si or Al improve the photoelectrochemical performance of α-Fe_2O_3. Therefore, we selected Ti, Si, and Al to investigate the effects of the incorporation of small amounts of these elements and combinations of them on thin film α-Fe_2O_3 photoanodes. Combinatorial printing templates such as those shown in Fig. 6.4 were created where the total amount of precursor deposited into each square is determined from the concentration of precursor salts in the printing solution, the drop volume of a printed drop, the number of layers printed and the number of drops inkjetted per unit area. This amount is determined by the areal density of dots and the number of ink-jetting nozzles actually firing on each printer cartridge. In the pattern, in Fig. 6.6b, four different densities of Fe and other metal (M = Ti, Si, or Al) were printed as double horizontal and double vertical rows, respectively, resulting in groups of four squares of nominally identical composition. The result of the photocurrent screening is shown in Fig. 6.6d–f.

Controlling the density of the printed drops allows the production of a quantifiable broad or narrow compositional range of dopant additions on each substrate. Table 6.2 contains the values of the drop spacings and densities used in Fig. 6.6d–f for the Fe and M (M = Ti, Si, or Al) oxide precursors taken individually. For example, the bottom four squares on the far left, corresponding to Fe_AM_D, were printed with a drop spacing of 160 μm for Fe (three layers) and 40 μm for M (M = Ti, Si, or Al for Fig. 6.6d, e and f, respectively). This set of squares corresponds to a nominal stoichiometry of $Fe_1M_{0.095}$ or 8.7% dopant, whereas the smallest percentage square corresponds to Fe_DM_A with a nominal stoichiometry of $Fe_1M_{0.00047}$ or 0.047% dopant. The corresponding numerical maximum IPCE data are summarized in Table 6.3. These values can be used to evaluate the relative responses when comparing the false color photocurrent scans since the brightest yellow shade was used to represent the maximum photocurrent response in each image. We found that in general only Ti-incorporation enhanced the photoelectrochemical performance

Table 6.3 Maximum IPCE data for Fig. 6.6c–f measured at two different biases

	Undoped Fig. 6.6c	Ti-doped Fig. 6.6d	Si-doped Fig. 6.6e	Al-doped Fig. 6.6f
0 V bias	2.60×10^{-4}	4.06×10^{-4}	2.58×10^{-4}	1.85×10^{-4}
+0.6 V bias	11.47×10^{-4}	15.54×10^{-4}	7.77×10^{-4}	6.02×10^{-4}

in comparison with an undoped iron oxide thin film, while the incorporation of Si or Al shows somewhat detrimental effects although there seems to be an increase in response for the thinner iron oxide films with the smallest amount of Si incorporation (Fe_ASi_A or $Fe_1Si_{0.0067}$ - bottom right corner of Fig. 6.6e) suggesting that perhaps even smaller additions of Si might improve the relative photoresponse. In previous work for films prepared by ultrasonic spray pyrolysis the corresponding nominal stoichiometry showing highly improved photoresponse is $Fe_1Si_{0.01}$ or ~1% dopant [37]. As for the Ti-doped iron oxide thin films, the best photocurrent response was observed at the relative stoichiometry of $Fe_1Ti_{0.025}$ while it ranges from $Fe_1Si_{0.0018}$ (or 0.18% dopant) to $Fe_1Si_{0.025}$ (or 2.4% dopant) for Si-doping, and $Fe_1Al_{0.0067}$ for Al-doping.

There have been numerous reports about the effects on photoelectrochemical response of incorporation of small amounts of the other elements into the binary α-Fe_2O_3 system. However, it is challenging to investigate the effects of adding multiple elements to α-Fe_2O_3 thin films especially if individual films have to be prepared at each stoichiometry. Our high-throughput combinatorial method can be used to quickly measure the effects of additions of multiple elements to find an optimal composition. Therefore we printed films with combinations of Ti, Si, and Al simultaneously added to α-Fe_2O_3. A printing template shown in Fig. 6.7 was created where four different densities of Ti and Si were printed as double horizontal and double vertical rows, respectively, and different amounts of Al were deposited in a repeating pattern within groups of four squares containing identical Fe, Ti, and Si amounts. The template was printed four times with different iron precursor drop spacings. The result is that the total thickness of the α-Fe_2O_3 decreases from Fig. 6.8a–d, whereas the relative concentration of the added dopants increases as we make the α-Fe_2O_3 film thinner. The top row of squares in the template are equal thickness squares of α-Fe_2O_3 where the first three pairs of squares have only one added metal dopant at the A and D levels (Al, Si, Ti left to right) with the far right pair of squares being just α-Fe_2O_3 printed at 40 and 160 μm spacings (Fe_D and Fe_A). Table 6.4 contains the values of drop spacings and drop densities used to print the template in Fig. 6.7 for the Fe–Ti–Si–Al oxide precursors. For illustrative purpose, the bottom square on the far left of the template, labeled $Si_DTi_AAl_B$, was printed with a drop spacing of 40, 160, and 120 μm for Si, Ti, and Al, respectively, while the Fe precursor was printed in three layers with different drop spacings of 40, 80, 120, 160 μm for Fig. 6.8a–d, respectively. So this lower left square in Fig. 6.8a–d will correspond to stoichiometries of $Fe_1Si_{0.0067}$-$Ti_{0.00047}Al_{0.00078}$, $Fe_1Si_{0.025}Ti_{0.0018}Al_{0.003}$, $Fe_1Si_{0.057}Ti_{0.0049}Al_{0.0067}$ and $Fe_1Si_{0.095}Ti_{0.0067}Al_{0.011}$, respectively. This printing pattern results in libraries of decreasing α-Fe_2O_3 thickness but increasing doping levels from Fig. 6.8a–d. The results of the photocurrent screening of these libraries are shown in Fig. 6.8a–d.

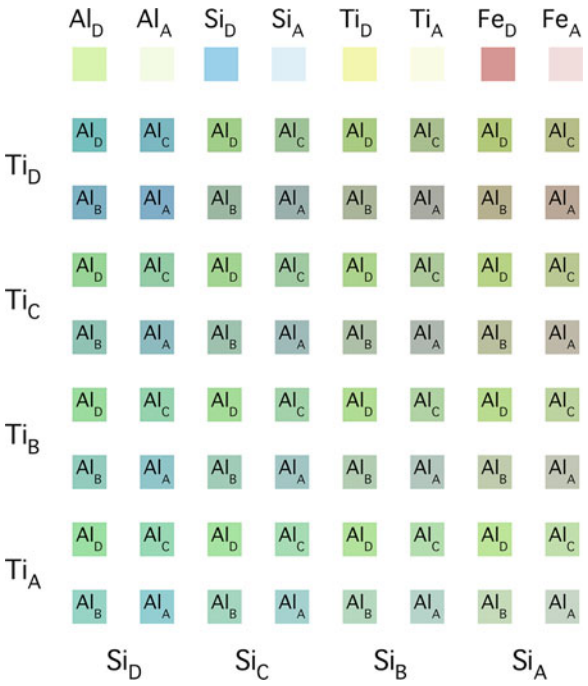

Fig. 6.7 Template used for the printed pattern in the Fe-Ti-Si-Al system where known amounts of the precursors are printed into individual 3 × 3 mm^2. The density of precursor drops and resulting stoichiometries for the various produced libraries are listed in Table 6.4

A series of pairs of internal standards consisting of undoped Fe and the Fe–Ti, Fe–Si, and Fe–Al binary systems with different drop densities (thickness) are also printed in the top row of the pattern as seen in Fig. 6.7.

IPCE values from the false color photocurrent data in Fig. 6.8a–d are summarized in Table 6.5. Again these values can be used to evaluate the relative responses when comparing the false color photocurrent scans since the brightest yellow shade was used to represent the maximum photocurrent response in each image. The highest overall IPCE data was obtained when the $FeCl_3$ precursor was printed three times with a drop spacing of 80 μm followed by drop spacings of 120, 40, and 160 μm (Figures 6.8b, c, a, and d, respectively). In Fig. 6.8a ($FeCl_3$ DS = 40 μm), the highest IPCE was observed at the Ti-rich area in this pattern ($Fe_1Ti_{0.0067}Si_xAl_x$ top two rows) but the overall thickness of this library was too large for efficient carrier harvesting revealed by the dark squares in the centers of the squares. Fig. 6.8b (DS = 80 μm) has the brightest spots when the relative stoichiometry is near $Fe_1Ti_{0.0067}Si_{0.0067}Al_x$ that occurs in the center section of the library. In Fig. 6.8c (DS = 120 μm) the relative stoichiometry of $Fe_1Ti_{0.0017}Si_xAl_x$ in the second set of double rows appears to have the highest photocurrent. It is quite interesting to observe there is tendency in Fig. 6.8d for the highest photocurrents appearing in the Al-rich areas with stoichiometry of $Fe_1Ti_xSi_xAl_{0.095}$. Another interesting aspect is that in all of the libraries the pure α-Fe_2O_3 (top right two squares) and the binary internal standards (top row pairs 1–3) almost always have a lower photocurrent response than the ternary additions in their respective libraries.

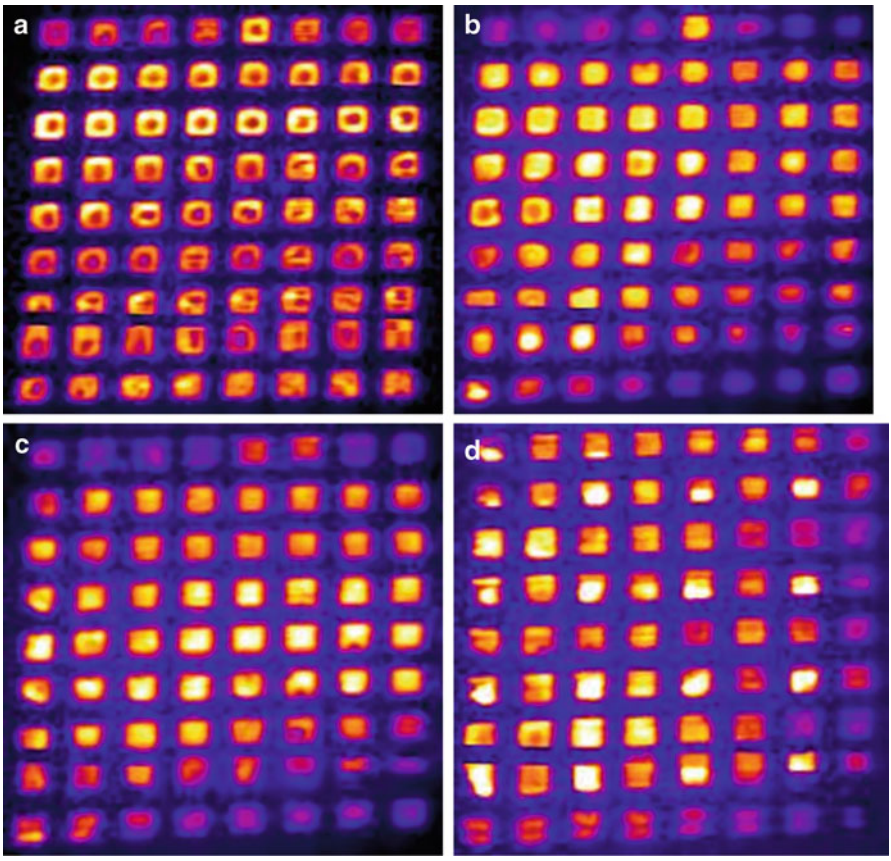

Fig. 6.8 (**a–d**) False color photocurrent maps with 532 nm laser excitation of the Fe–Ti–Si–Al system with no applied bias in a 0.1-M NaOH solution (Top Left $FeCl_3$ precursor drop spacings: $a = 40$ μm, $b = 80$ μm, $c = 120$ μm, $d = 160$ μm). Note that the false colors are relative within a scan and not absolute values therefore comparisons of color between scans are not quantitative. Refer to Table 6.5 for quantitative comparisons and the top row of standard squares with only one dopant or no dopant (see text)

Table 6.4 Density of printed precursor drops used to produce the mixtures shown in Fig. 6.8

Label	1D DS (μm)	Drops per mm^2	Relative stoichiometries (%)			
			$FeCl_3$, 3 × DS = 40 μm	$FeCl_3$, 3 × DS = 79 μm	$FeCl_3$, 3 × DS = 120 μm	$FeCl_3$, 3 × DS = 160 μm
D	40	642	0.67	2.5	5.7	9.5
C	79	169	0.17	0.67	1.5	2.5
B	120	75	0.078	0.3	0.67	1.1
A	160	45	0.047	0.18	0.49	0.67

The iron precursor ($FeCl_3$) was over-printed three times
DS drop spacing

Table 6.5 Summary of maximum IPCE data from Fig. 6.8

	Fig. 6.8a DS = 40	Fig. 6.8b DS = 80	Fig. 6.8c DS = 120	Fig. 6.8d DS = 160
0 V bias	2.36×10^{-4}	4.52×10^{-4}	4.15×10^{-4}	0.98×10^{-4}
+0.6 V bias	10.16×10^{-4}	15.54×10^{-4}	13.32×10^{-4}	6.26×10^{-4}

This indicates that there are synergistic effects of adding multiple dopants to the binary oxide semiconductor α-Fe_2O_3. As stated in the introduction this empirical study does not provide information about which of the many possible mechanisms for photocurrent improvement provided by the impurity is actually occurring in the α-Fe_2O_3 film. However, it does provide improved stoichiometries that should prove fruitful with more detailed studies of the actual electrical doping, morphological changes, carrier diffusion lengths and grain boundary and orientation effects attributable to the various impurities.

Due to the simplicity and low cost of the inkjet printing and screening protocols for discovering metal oxides capable of the photoelectrolysis of water, we embarked on a project to enlist multiple universities and even high schools in the search. We have produced the first beta printing and screening kits based on inexpensive components such as Lego Midstorms® kits, laser pointers and off-the-shelf inkjet printers that were distributed in the summer of 2008 to several universities with undergraduate summer research programs. The Solar Hydrogen Activity research Kit project (SHArK Project - www.thesharkproject.org) has recently expanded to over 20 sites world-wide and will be expanding to perhaps hundreds of sites in the near future. The SHArK Web site acts as a database of material combinations that have been investigated and as a communication tool for the various sites to exchange information. This "distributed research" project, initially funded by the Camille and Henry Dreyfus Foundation and now by the National Science Foundation, will lay the groundwork for a new generation of young scientists dedicated to helping solve the world energy problem.

6.4.3 Electrochemical Synthesis and Screening

To our knowledge McFarland et al. were the first to publish work on the combinatorial production of materials for water splitting. They demonstrated the electrochemical deposition of metal oxide compositions using robotics to electroplate and screen for water photooxidation activity individually created oxide materials using multiplexed photoelectrochemical cells [84]. Their work focused on variations in the electrochemical synthesis conditions, surface redox catalysts, control over structure [85] (by diverse surfactant and templating agents) and/or variable doping [86–88]. As illustrated in Fig. 6.9, the electrochemical deposition system utilizes a three-electrode electrochemical cell with coiled Pt and Ag wires serving as the

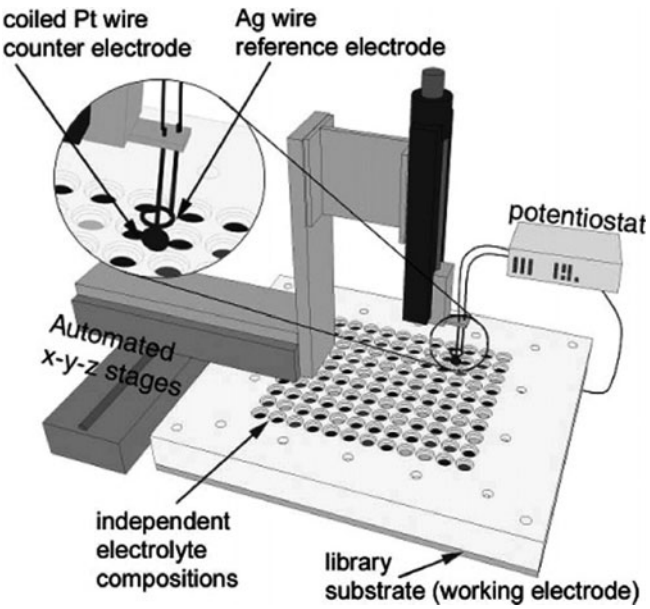

Fig. 6.9 An automated electrochemical deposition system used for the production of metal oxides. The custom-made well plate shown has been designed for a 120-sample array, each sealed by "O-rings" underneath a patterned Teflon block, and each containing a unique electrolyte composition. Reprinted with permission from [86], copyright 2005 American Chemical Society

counter and reference electrodes, respectively, that can be moved with a computer-controlled x–y–z stage. Metal ligand systems (citrates, peroxo complexes, etc.) or electrolyte conditions (pH and relative concentrations) are carefully designed to produce similar deposition potentials for the species in solution as the precursors are electrodeposited onto the conductive substrate (FTO or Ti) surface and then connected as the working electrode for evaluation in the sample well. The desired voltage, with a necessary overpotential to ensure deposition of both species, is applied at each well until a specified amount of charge has passed before moving the scanning electrodes to the next well.

In this high-throughput configuration, each cell is manually filled using a robotic pipetter before electrodeposition. Subsequent calcination produces mixtures of known stoichiometries that were verified by XPS measurements coupled to Ar^+ ion etching to examine the bulk and surface composition. Structural information was obtained with XRD. The screening system utilized for the electrochemically deposited samples incorporates measurements of flat-band potential, bias dependent photocurrent, and action spectra with a scanning photoelectrochemical probe [86]. Briefly, the probe steps from sample-to-sample across the library and an automated pump fills the probe with solution from a reservoir of stock electrolyte. An illuminated optical fiber targets each individual sample well and a three-electrode configuration is used to obtain photoelectrochemical data. A monochromator is placed between a chopped Xe lamp

and the optical waveguide for the IPCE measurements. Using the multiplexed photoelectrochemical screening system, the measured photoactivity of large bandgap materials for oxygen production, including ZnO [86] and WO_3 [84], and hydrogen production, including Al_2O_3 [72], has shown improvement after doping with certain elements around particular stoichiometries and complete photoelectrochemical information is obtained for each sample.

6.4.4 Sol Gel Routes

The recent work of Maier et al. [88, 89] has also added to the arsenal of combinatorial production and screening strategies to the search for novel hydrogen-producing photocatalysts, particularly for producing doped mixtures of compounds with sol gel precursors such as titanium. The reported technique incorporates computer-controlled pipetting robots to quantitatively dispense stock solutions of precursors into an array of small vials. When the pipetting process is finished, the samples are placed in an orbital shaker for mixing and a consistent aging, drying, and calcination protocol is followed for each sample to produce catalyst powders. The powders are then manually ground and suspended in an aqueous methanol solution in small gas chromatography (GC) vials. After flushing the headspace within the vials with an inert carrier gas, the GC sample holder is illuminated with a visible light source and the direct production of hydrogen gas can be monitored.

Using this method, after several generations of optimization, a newly discovered material, $Al_{40}Bi_{40}Pb_{20}O_x$, was identified for future studies. There are several problems associated with this technique, including the use of powders and sacrificial agents such as methanol, both of which were previously discussed. Nevertheless, it would be interesting to deploy the materials discovered by this technique as thin film photoelectrodes to test their photoelectrolysis activity.

6.4.5 Other Thin Film Deposition Techniques

Although they have not yet been applied to the production and screening of photoelectrolysis materials, we will briefly mention some other approaches to produce metal oxide libraries using well-established thin film deposition techniques (meant here to include physical vapor deposition, sputtering, pulsed laser deposition, and molecular beam epitaxy). These techniques have been used for the production of combinatorial metal oxide libraries in the search for more effective luminescent materials [90, 91], transparent conducting oxides [92, 93], and dielectrics [94, 95]. It would presumably be straightforward to apply the same techniques to the production of material libraries to be screened for photoelectrolysis activity.

6.5 From Materials Search to Bulk Photoelectrodes

Identification of stable semiconducting oxide materials with appropriate band gaps and band positions is only the first step toward a viable photoelectrolysis system. In general, two factors conspire to limit the photoconversion efficiency of oxide semiconductors. First, the optical transitions in these materials are usually forbidden d–d transitions and so they have much lower absorption coefficients when compared to direct bandgap semiconductors. The result is that light penetrates deeply into the material before being absorbed to create an electron hole pair. Other indirect photovoltaic materials such as Si have a similar absorption problem but it is overcome by having very long carrier lifetimes, resulting in long carrier diffusion lengths, so that photogenerated electrons and holes are eventually separated. Carriers in metal oxide semiconductor d-bands usually have very low mobilities due to the limited overlap between the metal d orbitals, resulting in shorter charge carrier diffusion lengths and increased bulk recombination of photogenerated carriers. Therefore, even if we could use costly single crystals of a metal oxide semiconductor, the carrier collection would be restricted to the narrow space charge layer where only a small fraction of the solar photons will be absorbed. Luckily, these same two problems have been solved by the architecture of the nanocrystalline dye-sensitized solar cell, that has reached laboratory efficiencies of over 10% compared to sensitized single crystals of the same oxide semiconductor that show a quantum yield of at most 1–2% due to the low light absorption of the monolayer of dye. Simply making the dye layer thicker does not solve the problem as excitons produced away from the dye/semiconductor interface recombine before they are separated due to the short exciton diffusion lengths in the organic dye layer. The high surface area morphology works to increase the effective optical absorption for these systems as the multitude of dye monolayers absorb all the light and inject their electrons into the TiO_2 conduction band and the holes (or oxidized dye molecules) are quickly scavenged by a regenerator (reducing agent) in solution. A similar nanostructured morphology is probably necessary for photoelectrolysis with metal oxides in order to compensate for the low absorption and carrier mobilities characteristic of metal oxide semiconductors with forbidden d–d optical transitions.

Another illustration of the importance of morphology in a metal oxide semiconductor uses α-Fe_2O_3 (hematite) as a photoelectrolysis material. Although iron (III) oxide is primarily used as a photoanode, it has been extensively studied to optimize its performance because it is inexpensive, easy to fabricate, has a bandgap (2.2 eV) that can absorb a good portion of the solar spectrum, and it is stable in aqueous solutions under illumination. High surface area nanostructured morphologies [96–98] of this material have been shown to more effectively harvest visible light relative to smooth films. For water cleavage, the best reported efficiencies (a solar-to-chemical conversion efficiency of 2.1%, based on the heat of hydrogen combustion), are achieved when used in a tandem configuration with a dye-sensitized solar cell.

The thickness of perpendicularly aligned α-Fe_2O_3 sheets is between 15 and 25 nm allowing for carrier diffusion to the surface. This morphology appears to be a critical parameter, since samples produced by different methods with similar thicknesses, crystal structure, and identical optical characteristics do not perform nearly as well. The authors argue that this particular grain size, orientation and morphology (leaf-shaped sheets) are required due to the short hole diffusion length of only a few nanometers for α-Fe_2O_3. This particular morphology affords facile transfer of holes to the electrolyte, before recombination occurs, while still shuttling electrons to the back contact. This morphology was produced using ultrasonic spray pyrolysis of their iron precursor solutions [86] to prepare their thin films. Addition of silicon produced further improvements in photoresponse again attributed to morphology changes rather than to electronic effects [84].

A nanostructured morphology also reduces the microscopic current density for water oxidation and reduction reactions resulting in lower overpotential losses than at a planar electrode. This will lower the electrocatalytic activity requirements for the semiconductor. In addition, many of the cell designs discussed herein or envisioned allow for thin nanostructured films deposited on a glass substrate with a transparent conducting layer. Such a configuration allows for back illumination, much like in the nanocrystalline solar cell. Back illumination of a photoelectrolysis electrode will reduce or eliminate the efficiency losses due to light scattering by the gas bubbles being evolved from the electrode surface.

6.6 Conclusions

We have surveyed the state of water photoelectrolysis using semiconductor electrodes and can conclude that there are currently no known suitable materials to efficiently and economically carry out this process. Due to the stability requirements we surmise that semiconducting oxide photoelectrodes are required. There are many potential oxide semiconductors that need to be prepared and tested for photoelectrolysis activity and therefore high-throughput combinatorial techniques are needed to discover promising materials. The first steps have been taken in the development of the combinatorial methods to solve this problem and these methods have been briefly reviewed. Optimization of the morphology of the semiconducting oxide thin film, probably with some kind of nanostructure, is required to overcome the limitations of light absorption and carrier transport in most oxide semiconductors. Mobilization of both experts and nonexpert researchers to discover and optimize new semiconductor materials is needed to produce the hydrogen needed to help move toward a clean energy economy based on renewable resources.

References

1. Ogden, J.M., Williams, R.H.: Electrolytic hydrogen from thin film solar cells. Int. J. Hydrogen Energy **15**, 155 (1990)
2. Boddy, P.J.: Oxygen evolution on potassium tantalate anodes. J. Electrochem. Soc. **115**, 199 (1968)
3. Fujishima, A., Honda, K.: Electrochemical evidence for the mechanism of the primary stage of photosynthesis. Bull. Chem. Soc. Jpn. **44**, 1148 (1971)
4. Fujishima, A., Honda, K.: Electrochemical photolysis of water at a semiconductor electrode. Nature **238**, 37 (1972)
5. Khaselev, O., Turner, J.A.: A monolithic photovoltaic-photoelectrochemical device for hydrogen production via water splitting. Science **280**, 425 (1998)
6. Rajeshwar, K.: Hydrogen generation at irradiated oxide semiconductor–solution interfaces. J. Appl. Electrochem. **37**, 765 (2007)
7. Bak, T., Nowotny, J., Rekas, M., Sorrell, C.C.: Photo-electrochemical hydrogen generation from water using solar energy. Materials-related aspects. Int. J. Hydrogen Energy **27**, 991 (2002)
8. Grimes, C.A., Varghese, O.K., Ranjan, S.: Light, water hydrogen. Springer, New York (2008)
9. Kung, H., Jarrett, H., Sleight, A., Ferretti, A.: Semiconducting oxide anodes in photoassisted electrolysis of water. J. Appl. Phys. **48**, 2463 (1977)
10. Wrighton, M.S., Ellis, A.B., Wolczanski, P.T., Morse, D.L., Abrahamson, H.B., Ginley, D.S.: Strontium titantate photoelectrodes: efficient photoassisted electrolysis of water at zero applied potential. J. Am. Chem. Soc. **98**, 2774 (1976)
11. Mavroides, J.G.: In: Heller, A. (ed.) Semiconductor liquid-junction solar cells. The Electrochemical Society, Princeton, NJ (1977)
12. Watanabe, I., Matsumoto, Y., Sato, E.: Photoelectrochemical properties of the single-crystal $SrTiO_3$ doped in the surface region. J. Electroanal. Chem. **133**, 359 (1982)
13. Mavroides, J.G., Kafalas, J.A., Kolesar, D.F.: Photoelectrolysis of water in cells with $SrTiO_3$ anodes. Appl. Phys. Lett. **28**, 241 (1978)
14. Nasby, R.D., Quinn, R.K.: Photoassisted electrolysis of water using a $BaTiO_3$ electrode. Mater. Res. Bull. **11**, 985 (1976)
15. Kennedy, J.H., Karl, J., Freese, W.: Photooxidation of water at barium titanate electrodes. J. Electrochem. Soc. **123**, 1683 (1976)
16. Harris, L.A., Wilson, R.H.: Semiconductors for photoelectrolysis. Annu. Rev. Mater. Sci. **8**, 99 (1978)
17. Hodes, G., Fonash, S.T., Heller, A., Miller, B.: In: Gerischer, H. (ed.) Advances in electrochemistry and electrochemical engineering. Wiley, New York (1985)
18. Rajeshwar, K., Singh, P., Dubow, J.: Energy conversion in photoelectrochemical systems – a review. Electrochim. Acta **23**, 1117 (1978)
19. Fan, F.R.F., White, H.S., Wheeler, B.L., Bard, A.J.: Semiconductor electrodes XXIX. High efficiency photoelectrochemical solar cells with n-WSe_2 electrodes in an aqueous iodide medium. J. Electrochem. Soc. **127**, 518 (1980)
20. Heller, A.: Conversion of sunlight into electrical power and photoassisted electrolysis of water in photoelectrochemical cells. Acc. Chem. Res. **14**, 154 (1981)
21. Strehlow, W.H., Cook, E.L.: J. Phys. Chem. Ref. Data **2**, 163 (1973)
22. Levy-Clement, C., Heller, A., Bonner, W.A., Parkinson, B.A.: Spontaneous photoelectrolysis of HBr and HI in two photoelectrode semiconductor liquid junction cells. J. Electrochem. Soc. **129**, 1701 (1982)
23. De, G.C., Roy, A.M., Bhattacharya, S.S.: Effect of n-Si on the photocatalytic production of hydrgen by Pt-loaded CdS and CdS/ZnS catalyst. Int. J. Hydrogen Energy **21**, 19 (1996)
24. Rauh, R.D., Buzby, J.M., Reise, T.F., Alkaitis, S.A.: Design and evolution of new oxide photoanodes for the photoelectroysis of water with solar energy. J. Phys. Chem. **83**, 2221 (1979)

25. Gerischer, H.: Photodecompostion of semiconductors, thermodynamics, kinetics, and applications to solar cells. Faraday Disc. **70**, 1A (1980)
26. Butler, M., Nasby, R., Quinn, R.: Tungsten trioxide as an electrode for photoelectrolysis of water. Solid State Commun. **19**, 1011 (1976)
27. Butler, M.A.: Photoelectrolysis and physical properties of the semiconducting electrode WO_3. J. Appl. Phys. **48**, 1914 (1977)
28. Berak, J.M., Sienko, M.J.: Effect of oxygen-deficiency on electrical transport properties of tungsten trioxide crystals. J. Solid State Chem. **2**, 109 (1970)
29. Wang, H., Lindgren, T., He, J., Hagfeldt, A., Lindquist, S.-E.: Photolelectrochemistry of nanostructured WO_3 thin film electrodes for water oxidation: mechanism of electron transport. J. Phys. Chem. B **104**, 5686 (2000)
30. Hardee, K., Bard, A.: Photoelectrochemical behaviour of several polycrystalline metal oxide electrodes in aqueous solutions. J. Electrochem. Soc. **123**, 1024 (1976)
31. Nasby, R., Quinn, R.: Photoassisted electrolysis of water using a $BaTiO_3$ electrode. Mater. Res. Bull. **11**, 985 (1976)
32. Kennedy, J.H., Frese, J.K.W.: Photooxidation of water at α-Fe_2O_3 electrodes. J. Electrochem. Soc. **125**, 709 (1978)
33. McGregor, K.G., Calvin, M., Otvos, J.W.: Photoeffects in Fe_2O_3 sintered semiconductors. J. Appl. Phys. **50**, 369 (1979)
34. Frelein, R.A., Bard, A.J.: Semiconductor electrodes XXI. The characterization and behavior of n-type Fe_2O_3 electrodes in acetonitrile solutions. J. Electrochem. Soc. **126**, 1892 (1979)
35. Wilhelm, S.M., Yun, K.S., Ballenger, L.W., Hackerman, N.: Semiconductor properties of iron oxide electrodes. J. Electrochem. Soc. **126**, 419 (1979)
36. Dare-Edwards, M.P., Goodenough, J.B., Hammett, A., Nicholson, N.D.: Photoelectrochemistry of NiO. J. Chem. Soc. Faraday Trans. **77**, 643 (1981)
37. Koffyberg, F.P., Benko, F.A.: A photoelectrochemical determination of the position of the conduction and valence band edges of p-type CuO. J. Electrochem. Soc. **128**, 2476 (1981)
38. Nikitine, S., Zielinger, J.P., Coret, A., Zouaghi, M.: Phys. Lett. **18**, 105 (1965)
39. Goodenough, J.B., Hamnett, A., Dare-Edwards, M.P., Campet, G., Wright, R.D.: Inorganic materials for photoelectrolysis. Surface Science **101**, 531 (1980)
40. Ishikawa, A., Takata, T., Kondo, J., Hara, M., Kobayashi, H., Domen, K.: Oxysulfide $Sm_2Ti_2S_2O_5$ as a stable photocatalyst for water oxidation and reduction under visible light irradiation. J. Am. Chem. Soc. **124**, 13547 (2002)
41. Hitoki, G., Takata, T., Kondo, J.N., Hara, M., Kobayashi, H., Domen, K.: Ta_3N_5 as a novel visible light-driven photocatalyst. Chem. Commun. 1698 (2002).
42. Liu, M., You, W. Lei, Z., Zhou, G., Yang, J., Wu, G., Ma, G., Luan, G., Takata, T., Hara, M., Domen, K., Li, C.: Water reduction and oxidation on Pt-Ru/$Y_2Ta_2O_5N_2$ catalyst under visible light irradiation. Chem. Commun. 2192 (2004).
43. Hitoki, G., Ishikawa, A., Takata, T., Kondo, J., Hara, M., Domen, K.: Ta_3N_5 as a novel visible light-driven photocatalyst. Chem. Lett. **1**, 736 (2002)
44. Kasahara, A., Nukumizu, K., Hitoki, G., Takata, T., Kondo, J., Hara, M., Kobayashi, H., Domen, K.: Photoreactions on $LaTiO_2N$ under visible light irradiation. J. Phys. Chem. A **106**, 6750 (2002)
45. Kasahara, A., Nukumizu, K., Takata, T., Kondo, J., Hara, M., Kobayashi, H., Domen, K.: $LaTiO_2N$ as a visible light driven photocatlayst. J. Phys. Chem. B **107**, 791 (2003)
46. Yu, J.C., Zhang, L., Zheng, Z., Zhao, J.: Synthesis and characterization of phosphated mesoporous titanium dioxide with high photocatalytic activity. Chem. Mater. **15**, 2280 (2003)
47. Asahi, R., Morikawa, T., Ohwaki, T., Aoki, K., Taga, Y.: Visible light photocatalysts in nitrogen-doped titanium oxides. Science **293**, 269 (2001)
48. Serpone, N.: Is the band Gap of pristine TiO_2 narrowed by anion and cation doping of titanium dioxide in second generation photocatalysts. J. Phys. Chem. B **110**, 24287 (2006)
49. Livraghi, S., Paganini, M.C., Giamello, E., Selloni, A., Valentin, C.D., Pacchioni, G.: Origin of photoactivity of nitrogen doped titanium dioxide under visible light. J. Am. Chem. Soc. **128**, 15666 (2006)

50. Bin-Daar, G., Dare-Edwards, M.P., Goodenough, J.B., Hamnett, A.: New anode materials for photolectrolysis. J. Chem. Soc. Faraday Trans. **79**, 1199 (1983)
51. Jarrett, H.S., Sleight, A.W., Kung, H.H., Gillson, J.L.: Photoelectrochemical and solid-state properties of $LuRhO_3$. J. Appl. Phys. **51**, 3916–3925 (1980)
52. Guruswamy, V., Keillor, P., Campbell, G.L., Bockris, J.O.M.: The photoelectrochemical response of the lanthanides of chromium, rhodium, vandium, and gold on a titanium base. Sol. Energ. Mater. Sol. Cell. **4**, 11 (1980)
53. Takata, T., Shinohara, K., Tanaka, A., Hara, M., Kondo, J., Domen, K.: Photocatalytic decomposition of water on spontaneously hydrated layered perovskites. J. Photochem. Photobiol. **106**, 45 (1997)
54. Yoshimura, J., Ebina, Y., Kondo, J., Domen, K.: Visible light induced photocatalytic behavior of a layered perovskite type niobate, $RbPb_2Nb_3O_{10}$. J. Phys. Chem. **97**, 1970 (1993)
55. Ghosh, A.K., Maruska, P.: Photoelectrolysis of water in sunlight with sensitized semiconductor electrodes. J. Electrochem. Soc. **124**, 1516 (1977)
56. Kato, H., Kudo, A.: Visible light response and photocatalyltic activities of TiO2 and $SrTiO_3$ photocatalyts Co doped with antimony and chromium. J. Phys. Chem. B **106**, 5029 (2002)
57. Ishii, T., Kato, H., Kudo, A.: H_2 evolution from an aqueous methanol solution on $SrTiO_3$ photocatalyts codoped with chromium and tantalum ions under visible light irradiation. J. Photochem. Photobiol. A **163**, 181 (2004)
58. Woodhouse, M., Parkinson, B.A.: Combinatorial discovery and optimization of a complex oxide with water photoelectrolysis activity. Chem. Mater. **20**, 2495 (2008)
59. Tsuji, I., Kato, H., Kobayashi, H., Kudo, A.: Photocatalytic H_2 evolution reaction from aqueous solutions over band controlled $AgIn_xZn_{2-x}S_2$ solid solution photocatalyts with visible light response and their surface nanostructures *J*. Am. Chem. Soc. **126**, 13406 (2004)
60. Zou, Z., Ye, J., Sayama, K., Arakawa, H.: Direct splitting of water under visible light irradiation with an oxide semiconductor photocatalyst. Nature **414**, 625 (2001)
61. Kudo, A., Kato, H.: Effect of lanthanide doping into $NaTaO_3$ photocatalyts for efficient water splitting. Chem. Phys. Lett. **331**, 373 (2000)
62. Reddington, E., Sapienza, A., Gurau, B., Viswanathan, R., Sarangapeni, S., Smotkin, E.S., Mallouk, T.E.: Combinatorial electrochemistry: a highly parallel, optical screening method for discovery of better electrocatalysts. Science **280**, 1735 (1998)
63. Morris, N.D., Mallouk, T.E.: A high-throughput optical screening method for the optimization of colloidal water oxidation catalysts. J. Am. Chem. Soc. **124**, 11114 (2002)
64. Chen, L., Bao, J., Gao, C.: Combinatorial synthesis of insoluble oxide library from ultrafine/nanoparticle suspension using a drop on demand inkjet delivery system. J. Comb. Chem. **6**, 699 (2004)
65. Woodhouse, M., Herman, G., Parkinson, B.A.: Combinatorial approach to identification of catalysts for the photoelectrolysis of water. Chem. Mater. **17**, 4318 (2005)
66. Katz, J.: Metal oxide based photoelectrochemical cells for solar energy conversion. PhD Thesis, California Institute of Technology, Pasadena, CA (2007)
67. Arai, T., Konishi, Y., Iwasaki, Y., Sugihara, H., Sayama, K.: High throughput screening using porous photoelectrodes for the development of visible-light responsive semiconductors. J. Comb. Chem. **9**, 574 (2007)
68. Sartoretti, C.J., Alexander, B.D., Solarska, R., Rutkowska, W.A., Augustynski, J., Cerny, R.: Photoelectrochemical oxidation of water at transparent ferric oxide film electrodes. J. Phys. Chem. B **109**, 13685 (2005)
69. Kay, A., Cesar, I., Gratzel, M.: A new benchmark for water photooxidation by nanostructured Fe_2O_3 films. J. Am. Chem. Soc. **128**, 15714 (2006)
70. Murphy, A.B., Barnes, P.R.F., Randeniya, L.K., Plumb, I.C., Grey, I.E., Horne, M.D., Glasscock, J.A.: Efficiency of solar water splitting using semiconductor electrodes. Int. J. Hydrogen Energy **2006**, 31 (1999)
71. Mohanty, S., Ghose, J.: Studies on some α-Fe_2O_3 photoelectrodes. J. Phys. Chem. Solids **53**, 81 (1992)

72. Glasscock, J.A., Barnes, P.R.F., Plumb, I.C., Savvides, N.: Enhancement of photoelectrochemical hydrogen production from hematite thin films by the introduction of Ti and Si. J. Phys. Chem. C **111**, 16477 (2007)
73. Arai, T., Konishi, Y., Iwasaki, Y., Sugihara, H., Sayama, K.: High throughput screening using porous photoelectrodes for the development of visible-light responsive semiconductors. J. Comb. Chem. **9**, 574 (2007)
74. Shinar, R., Kennedy, J.H.: Iron oxide photoanaodes. Sol. Energy Mater. **6**, 323 (1982)
75. Leygraf, C., Hendewerk, M., Somorjai, G.A.: Photodissociation of water by p- and n-type polycrystalline iron oxides by using visible light ($\leq$2.7 eV) in the absence of external potential. Proc. Natl. Acad. Sci. U.S.A. **79**, 5739 (1982)
76. Turner, J.E., Hendewerk, M., Parmeter, J., Neiman, D., Somorjai, G.A.: The characterization of doped iron oxide electrodes for the photodissociation of water. J. Electrochem. Soc. **131**, 1777 (1984)
77. Khader, M.M., Vurens, G.H., Kim, I.K., Salmeron, M., Somorjai, G.A.: Photoassisted catalytic dissociation of water to produce hydrogen on partially reduced alpha.-iron(III) oxide. J. Am. Chem. Soc. **109**, 3581 (1987)
78. Bjorksten, U., Moser, J., Gratzel, M.: Photoelectrochemical studies on nanocrystalline hematite films. Chem. Mater. **6**, 858 (1994)
79. Duret, A., Gratzel, M.: Visible light-induced water oxidation on mesoscopic α-Fe_2O_3 films made by ultrasonic spray pyrolysis. J. Phys. Chem. B **109**, 17184 (2005)
80. Aroutiounian, V.M., Arakelyan, V.M., Shahnazaryan, G.E., Stepanyan, G.M., Khachaturyan, E.A., Wang, H., Turner, J.A.: Investigations of the metal-oxide semiconductors promising for photoelectrochemical conversion of solar energy. Sol. Energy **80**, 1098 (2006)
81. Hu, Y.S., Kleiman-Shwarcstein, A., Forman, A.J., Hazen, D., Park, J.N., McFarland, E.W.: Pt-doped α-Fe_2O_3 thin films active for photoelectrochemical water splitting. Chem. Mater. **20**, 3803 (2008)
82. Kleiman-Shwarsctein, A., Hu, Y.S., Forman, A.J., Stucky, G.D., McFarland, E.W.: Electrodeposition of α-Fe_2O_3 doped with Mo or Cr as photoanodes for photocatalytic water splitting. J. Phys. Chem. C **112**, 15900 (2008)
83. Cesar, I., Kay, A., Cesar, I., Martinez, J.A.G., Grätzel, M.: Translucent thin film Fe_2O_3 photoanodes for efficient water splitting by sunlight: nanostructure-directing effect of Si doping. J. Am. Chem. Soc. **128**, 4582 (2006)
84. Baeck, S.H., Jaramillo, T.F., Brandli, C., McFarland, E.W.: Combinatorial electrochemical synthesis and characterization of tungsten-based mixed metal oxides. J. Comb. Chem. **4**, 563 (2002)
85. Jaramillo, T.F., Baeck, S.-H., Kleiman-Shwarsctein, A., McFarland, E.W.: Combinatorial electrochemical synthesis and screening of mesoporous ZnO for photocatalysis. Macromol. Rapid Commun. **25**, 297 (2004)
86. Jaramillo, T.F., Baeck, S.-H., Kleiman-Shwarsctein, A., Choi, K.-S., Stucky, G.D., McFarland, E.W.: Automated electrochemical synthesis and photoelectrochemical characterization of Zn-Co-oxide thin films for solar hydrogen production. J. Comb. Chem. **7**, 264 (2005)
87. Jaramillo, T.J., Ivanovskaya, A., McFarland, E.W.: High throughput screening system for catalytic hydrogen producing materials. J. Comb. Chem. **4**, 17 (2002)
88. Seyler, M., Stoewe, K., Maier, W.F.: New hydrogen producing photocatalysts – a combinatorial search. Appl Cat. B **76**, 146 (2007)
89. Lettmann, C., Hinrichs, H., Maier, W.F.: Combinatorial discovery of new photocatalysts for water purification with visible light. Angew. Chem. Int. Ed. **40**, 3160 (2001)
90. Takeuchi, I., Lauterbach, J., Fasolka, M.J.: Combinatorial synthesis and evaluation of functional inorganic materials using thin-film techniques. Mater. Today **8**, 18 (2005)
91. Wang, J., Yoo, Y., Gao, C., Takeuchi, I., Sun, X., Chang, H., Xiang, X.-D., Schultz, P.G.: Identification of a blue photoluminiscent composite material from a combinatorial library. Science **279**, 1712 (1998)

92. Hest, M.F.A.M.v., Dabney, M.S., Perkins, J.D., Ginley, D.S., Taylor, M.P.: Titanium-doped indium oxide: a high-mobility transparent conductor. Appl. Phys. Lett. **87**, 032111 (2005).
93. Hest, M.F.A.M.v., Dabney, M.S., Perkins, J.D., Ginley, D.S.: High-mobility molybdenum doped indium oxide. Thin Solid Films **496**, 70 (2006).
94. Dover, R.B.v., Schneemeyer, L.F., Fleming, R.M.: Discovery of a useful thin-film dielectric using a composition spread approach. Nature **392**, 162 (1998).
95. Dover, R.B.v., Schneemeyer, L.F.: The codeposited composition spread approach to high-throughput discovery/exploration of inorganic materials. Macromol. Rapid Commun. **25**, 150 (2004).
96. Cesar, I., Kay, A., Martinez, J.A.G., Gratzel, M.: Translucent thin film Fe_2O_3 photoanodes for efficient water splitting by sunlight: nanostructure-directing effect of Si doping. J. Am. Chem. Soc. **128**, 4582 (2006)
97. Sartoretti, C.J., Alexander, B.D., Solarska, R., Rutkowska, I.A., Augustynski, J., Cerny, R.: Photoelectrochemical oxidation of water at transparent ferric oxide film electrodes. J. Phys. Chem. B **109**, 13685 (2005)
98. Duret, A., Gratzel, M.: Visible light-induced water oxidation on mesoscopic α-Fe_2O_3 films made by ultrasonic spray pyrolysis. J. Phys. Chem. B **109**, 17184 (2005)